

Localized and extended patterns in the cubic-quintic Swift-Hohenberg equation on a disk

Nicolás Verschueren^{*} and Edgar Knobloch[†]

Physics Department, University of California at Berkeley, Berkeley CA 94720, USA

Hannes Uecker[‡]

Institute for Mathematics, Carl von Ossietzky University of Oldenburg, Oldenburg, Germany

(Dated: February 2, 2022)

Axisymmetric and nonaxisymmetric patterns in the cubic-quintic Swift-Hohenberg equation posed on a disk with Neumann boundary conditions are studied via numerical continuation and bifurcation analysis. Axisymmetric localized solutions in the form of spots and rings known from earlier studies persist and snake in the usual fashion until they begin to interact with the boundary. Depending on parameters, including the disk radius, these states may or may not connect to the branch of domain-filling target states. Secondary instabilities of localized axisymmetric states may create multi-arm localized structures that grow and interact with the boundary before broadening into domain filling states. High azimuthal wavenumber wall states referred to as daisy states are also found. Secondary bifurcations from these states include localized daisies, i.e., wall states localized in both radius and angle. Depending on parameters, these states may snake much as in the one-dimensional Swift-Hohenberg equation, or invade the interior of the domain, yielding states referred to as worms, or domain-filling stripes.

I. INTRODUCTION

Pattern formation is a familiar feature of many physical, chemical and biological systems. Patterns generally form as a result of a symmetry-breaking instability of a spatially homogeneous state. The simplest situation arises on an infinite domain in one, two, or three space dimensions (1D, 2D or 3D, respectively), since this formulation admits spatially periodic structures. These persist when the domain is replaced by a periodic domain, or with some restrictions, by a domain with Neumann boundary conditions. The subject is reviewed in the books by Hoyle [1] and Cross and Greenside [2]. However, in most applications, particularly in fluid dynamics and chemical systems, the presence of lateral boundaries becomes of fundamental importance. This paper is devoted to the explanation of pattern formation on perhaps the simplest bounded domain in 2D, the finite disk, focusing on phenomena associated with subcritical instabilities of the homogeneous state, i.e., associated with the presence of bistability between the homogeneous state and different pattern states.

For this purpose we select the simplest pattern-forming equation, the Swift–Hohenberg (SH) equation, a dissipative evolution equation for a scalar field $u(\mathbf{x}, t)$ in 2D. The equation is characterized by a finite wave number instability that takes place, in an infinite system, at $\varepsilon = 0$, where ε is the bifurcation parameter. Because of its variational structure, all time-dependence ultimately dies out, allowing us to focus on time-independent solutions. We

choose the nonlinear terms to be of cubic-quintic type in order to allow for bistability between the homogeneous state $u = 0$ and a stripe-like pattern. This type of equation arises as a plausible model of many systems, particularly those arising in fluid dynamics, although a rigorous derivation is lacking [3]. However, because of its simplicity the equation has been the model of choice for many pattern formation studies, and this is the case in the present contribution as well.

In the case of a finite disk, two basic types of localized states occur: states localized in the interior of the domain, and states localized near its boundary. The former behave much like analogous structures in the plane, at least until they have grown to such a size that they begin to interact with the boundary. In contrast, the latter, referred to here as wall states, are present only because of the boundary, and so have no analogue in the infinite plane. We focus here on understanding the basic properties of these solutions and their interaction as parameters are varied, as well as on their interaction with coexisting domain-filling structures such as target states and other stripe-like states. The former are parallel to the boundary, while the latter are frequently perpendicular to it. Periodic wall states are also of special interest. We refer to these as daisy states, and since these also bifurcate subcritically, we expect the presence of azimuthally localized daisy states resembling partially plucked daisies. We find that these states do indeed exist and that they snake, for moderate subcriticality, much like the localized states in the 1D cubic-quintic SH equation. However, this ceases to be the case for stronger subcriticality, for which the localized daisies expand into the domain interior instead of expanding along the boundary. Figure 1 illustrates some of the solutions studied in this paper.

Some of our patterns resemble states generated in supercritical steady state bifurcations from a trivial state

^{*} nverschueren@berkeley.edu

[†] knobloch@berkeley.edu

[‡] hannes.uecker@uni-oldenburg.de

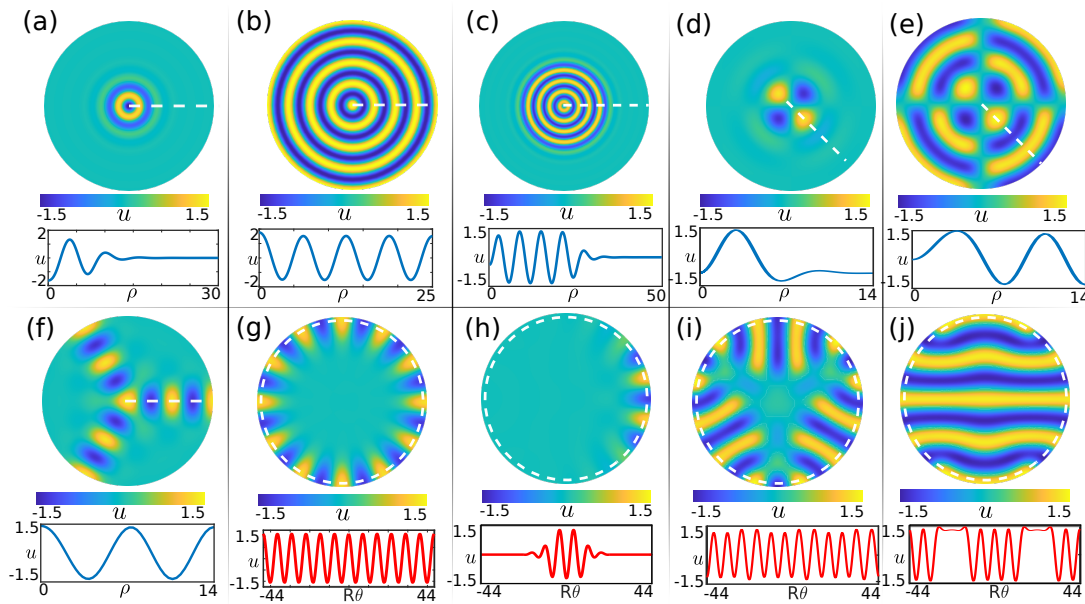


FIG. 1. States observed in Eq. (1) with the boundary conditions (2), $q = 1$. (a) Spot $(R, \varepsilon, \nu) = (30, -0.580, 2)$, (b) target $(R, \varepsilon, \nu) = (25, -0.780, 2)$, (c) ring state $(R, \varepsilon) = (50, -0.650, 2)$, (d) 4^- -arm localized state $(R, \varepsilon, \nu) = (14, -0.5980, 2)$, (e) 4^- -arm extended state $(R, \varepsilon, \nu) = (14, -0.6460, 2)$, (f) 3^+ -arm state $(R, \varepsilon, \nu) = (14, -0.7048, 2)$, (g) daisy state $(R, \varepsilon, \nu) = (14, -0.353, 1.5)$, (h) plucked daisy state $(R, \varepsilon, \nu) = (14, -0.3231, 1.5)$, (i) worm-like state $(R, \varepsilon, \nu) = (14, -0.2755, 1.4)$, and (j) stripe-like state $(R, \varepsilon, \nu) = (14, -0.6, 2)$. Each state is accompanied in a lower panel by a 1D profile along the dashed white line in the panel above; in (g)-(j) this line is slightly displaced from the perimeter for ease of visibility.

on a disk, for instance in convection in a cylinder [4–9] and in flame dynamics above a circular burner [10]. However, in these systems spatial localization is generally absent, because roll convection sets in supercritically (the midplane or Boussinesq symmetry of this system precludes subcritical hexagons at onset) while combustion away from onset also behaves like a supercritical system. Near onset, however, ignition is often subcritical, a fact that may be responsible for the appearance of localized hotspots and flickering in this regime [11]. Related structures are also seen in reaction-diffusion systems on a disk [12], and in vertical cavity surface emitting lasers (VCSELs) with a round aperture [13].

Localized wall modes are present in rotating convection in a cylinder [14, 15]; these modes precess in a retrograde fashion, and in the strongly nonlinear regime appear to be responsible for the boundary zonal flows observed in experiments at high Rayleigh number (strong forcing) [16]. Similar rotating states are present even in nonrotating Rayleigh-Bénard convection but appear via a symmetry-breaking Hopf bifurcation from an axisymmetric state [17]. However, such dynamical states cannot be described by variational systems such as the SH equation with Neumann boundary conditions, although both mixed (i.e., Robin) boundary conditions [18] or the so-called spiral boundary conditions [19] admit the presence of Hopf bifurcations and hence persistent dynamics.

The remainder of the paper is organized as follows. Section II introduces the model, emphasizing symme-

tries, effective number of parameters, and variational structure. In addition, linear stability properties of the $u = 0$ state are determined and thresholds for different types of instabilities are identified. Sections III and IV describe the results of numerical continuation of some of the steady states generated by these unstable modes, focusing on two distinct types of solutions, namely axisymmetric solutions [Fig. 1(a)-(c)] and nonaxisymmetric solutions that include m -arm states [Fig. 1(d)-(f)], wall-mode states [Fig. 1(g),(h)] and worms and stripes [Fig. 1(i),(j)]. The axisymmetric states are studied in Sec. III via solutions of a nonautonomous boundary value problem in the radial coordinate ρ , and their relation to the results on an unbounded domain [20–22] is explored. Section IV describes the organization of nonaxisymmetric solutions on the disk, which we classify into multi-arm solutions and daisy states. Bifurcations from daisy states yield localized daisies, and for moderate subcriticality the associated branches closely resemble the classical 1D snakes-and-ladders scenario [23]. However, these snakes break up with increased subcriticality, leading to worm states at the wall. Section V shows a comparison between the solution branches in terms of the free energy, while Sec. VI illustrates additional patterns that are also present. The paper concludes in Sec. VII with a discussion and suggestions for future work. An Appendix contains some details on the numerics, and further information, including movies stepping through some of the bifurcation diagrams, is provided in the Supplementary

Information (SI).

II. THE MODEL

We consider the SH model with a cubic-quintic nonlinearity,

$$\partial_t u = \varepsilon u + \nu u^3 - u^5 - (q^2 + \Delta)^2 u, \quad (1)$$

where $u(\mathbf{x}, t)$ is a real-valued scalar field and ε, ν and q are parameters. In contrast to much of the earlier literature, here the equation is posed on a disk of radius R subject to the boundary conditions

$$\nabla u \cdot \hat{n}|_{\partial\Omega} = 0, \quad \nabla(\Delta u) \cdot \hat{n}|_{\partial\Omega} = 0, \quad (2)$$

referred to as Neumann boundary conditions. We solve this problem on two distinct domains, a finite disk Ω_1 of radius R illustrated in Fig. 2(a) and a sector Ω_2 of opening angle $2\phi_0$ illustrated in Fig. 2(b):

$$\Omega_1 = \{\mathbf{x} \in (\rho, \phi) \in \mathbb{R}^2 | \rho \in [0, R], \phi \in [0, 2\pi]\}, \quad (3a)$$

$$\Omega_2 = \{\mathbf{x} \in (\rho, \phi) \in \mathbb{R}^2 | \rho \in [0, R], \phi \in [-\phi_0, \phi_0]\}. \quad (3b)$$

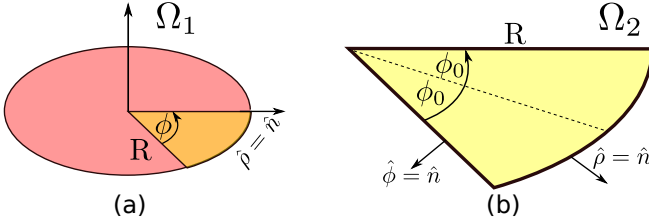


FIG. 2. The domains Ω_1 and Ω_2 defined in Eqs. (3a) and (3b) showing the normal vector \hat{n} .

In the following the symmetry $u \rightarrow -u$ of Eq. (1) will play a fundamental role. Although the problem is specified by four parameters, ε, ν, q, R , we can without loss of generality set $q = 1$ since other values of q can be accommodated by the rescaling

$$\Delta = q^2 \Delta', \quad u = qu', \quad \partial_t = q^4 \partial_{\tau'}, \quad \varepsilon = \varepsilon' q^4, \quad \nu = \nu' q^2. \quad (4)$$

Thus R is measured in units of q^{-1} .

The model (1), posed on the finite disk Ω_1 with the boundary conditions (2), possesses variational structure. More precisely, the free energy

$$\mathcal{F}[u] \equiv \int_{\Omega} \left(\frac{1}{2} [(q^2 + \Delta)u]^2 - \frac{\varepsilon}{2} u^2 - \frac{\nu}{4} u^4 + \frac{1}{6} u^6 \right) d\mathbf{x}, \quad (5)$$

satisfies, on using integration by parts and the boundary conditions,

$$\begin{aligned} \frac{d\mathcal{F}}{dt} &= \int_{\Omega} [-\varepsilon u - \nu u^3 + u^5 + q^2((q^2 + \nabla^2)u)] (\partial_t u) d\mathbf{x} \\ &\quad + \int_{\Omega} ((q^2 + \nabla^2)u) \nabla^2(\partial_t u) d\mathbf{x} \\ &= - \int_{\Omega_1} (\partial_t u)^2 d\mathbf{x}. \end{aligned} \quad (6)$$

Since $\mathcal{F}[u]$ is bounded from below, it decreases along trajectories until $\partial_t u = 0$. The variational structure of Eqs. (1)–(2) thus rules out persistent dynamics and we therefore focus on time-independent solutions of the problem.

Our main tool for exploring time-independent solutions of (1) is numerical continuation. We make extensive use of the packages AUTO [24] and pde2path [25–27]. For numerical continuation in 2D, the number of states often increases rapidly with the size of the domain and branch jumping, i.e., uncontrolled and undetected switching of states from one solution branch to another, becomes a problem in the neighborhood of bifurcation points. One strategy to mitigate this problem is to employ symmetries to restrict the study to a smaller domain, a procedure that also reduces numerical effort. See [26, §3.6.1, §8.3.1] for further comments. Here we fix a moderate value for the disk radius and in some settings study the problem on the sectorial domain (3b) instead of the whole disk (3a). For the opening angle $2\phi_0$ we take $\phi_0 = \pi/n$ with n an integer and impose Neumann boundary conditions along $\phi = \pm\phi_0$ in addition to $r = R$.

A. Linear stability of the trivial state $u = 0$

The linearization of (1) about the homogeneous solution $u = 0$ reads

$$\partial_t v = [\varepsilon - (q^2 + \Delta)^2]v, \quad |v| \ll 1. \quad (7)$$

Equation (7) can be solved via separation of variables, using the eigenfunctions of the Laplacian in polar coordinates (ρ, ϕ) , i.e., we seek solutions of the form $v(\rho, \phi, t) = e^{\sigma t} w(\rho, \phi)$ with

$$w(\rho, \phi) = J_m(k\rho) \cos(m\phi + \alpha), \quad (8)$$

where σ, α and k are constants to be determined for each value of the azimuthal wave number $m \in \mathbb{N}_0$. Substituting $v(\rho, \phi, t)$ into (7) yields the dispersion relation

$$\sigma = \varepsilon - (q^2 - k^2)^2. \quad (9)$$

Instability sets in when σ crosses zero. The resulting critical case $\sigma = 0$ admits four values of k , $k_{\pm, \pm} = \pm\sqrt{q^2 \pm \sqrt{\varepsilon}}$. However, with $m \in \mathbb{N}_0$ it follows that $J_m(-x) = (-1)^m J_m(x)$ and consequently that only two of these solutions are linearly independent. Thus

$$w(\rho, \phi) = (A_m J_m(k_+ \rho) + B_m J_m(k_- \rho)) \cos(m\phi + \alpha) \quad (10)$$

where $k_{\pm} = \sqrt{q^2 \pm \sqrt{\varepsilon}}$. In order to determine the constants A_m, B_m and α , we impose the boundary conditions (2). In the case of the full disk (domain Ω_1), the solution must be periodic in the angular variable ϕ , implying that $m \in \mathbb{N}_0$. In the case of a slice of half-angle $\phi_0 = \pi/n$ (domain Ω_2 with $1 < n \in \mathbb{N}$), the boundary conditions in the angular coordinate yield

$$\sin\left(m\frac{\pi}{n} + \alpha\right) = 0,$$

which can be satisfied by either

$$\alpha = 0, \quad m = ln, \quad \text{or} \quad \alpha = \frac{\pi}{2}, \quad m = \frac{(2l-1)n}{2}, \quad l \in \mathbb{N}_0,$$

where without loss of generality we take $l = 1$. We interpret this result as follows. Either $n = m$ in which case n copies of the solution generate an m -fold solution on the whole disk, or $n = 2m$ implying that one must first double the domain via reflection in $\phi = \phi_0$ or $\phi = -\phi_0$ before replicating the result to obtain an $m = n/2$ -fold state [28]. Thus n is an even integer, and solutions of this type with n odd are not solutions on the whole disk.

The boundary conditions at $\rho = R$ are the same for both the full disk and the sector: these yield a set of two linear equations for A_m, B_m given by

$$\mathbb{M} \begin{pmatrix} A_m \\ B_m \end{pmatrix} = \begin{pmatrix} 0 \\ 0 \end{pmatrix}, \quad \mathbb{M} \equiv \begin{pmatrix} k_+ J'_m(k_+ R) & k_- J'_m(k_- R) \\ k_+^3 J'_m(k_+ R) & k_-^3 J'_m(k_- R) \end{pmatrix}.$$

To find nontrivial solutions of this equation for given m and R we determine ε from

$$\det(\mathbb{M}) = 2\sqrt{\varepsilon} \sqrt{q^4 - \varepsilon} J'_m(k_+ R) J'_m(k_- R) = 0. \quad (11)$$

If $\varepsilon = 0$, then $k_- = k_+ > 0$, and condition (11) is satisfied trivially. In this case Eq. (9) shows that no instability takes place. Similarly, $\varepsilon = q^4$ also satisfies (11) for all m . We disregard this case because we are interested in small values of ε and $q \sim O(1)$. Condition (11) thus reduces to

$$J'_m(k_+ R) J'_m(k_- R) = 0.$$

In order to illustrate the predictions from this condition, we consider the cases $q = 1$, $\phi_0 = \frac{\pi}{2}$ (half disk) and $R = 14$ and $R = 15$ (Fig. 3). Using computer algebra we find the first six values of ε satisfying (11). On the full disk, we obtain the same eigenvalues, but for $m \neq 0$ these are of double multiplicity.

The values found are in good agreement with the bifurcation points found from one-parameter numerical continuation of the trivial state $u = 0$ of (1) on the half disk. The percentage difference between the predicted and observed values of ε is always under 1%. Figure 3 illustrates the first six predicted (and numerically computed) eigenvectors when $R = 14$ and $R = 15$, sorted by the corresponding eigenvalues ε . Remarkably, the only mode that is common to both lists is $m = 3$, indicating a strong dependence on R of the initial bifurcation sequence. Although the number of possibilities increases rapidly with the domain size, we can always identify two qualitatively different types of eigenvectors: *Axisymmetric* solutions characterized by $m = 0$ (when $R = 14$ these appear at $\varepsilon_5 \approx 8.88 \times 10^{-3}$, Fig. 3(a); when $R = 15$ the onset of axisymmetric states is delayed to $\varepsilon_{13} \approx 4.20 \times 10^{-2}$ and $\varepsilon_{14} \approx 4.50 \times 10^{-2}$, i.e., two such modes arise in close succession) and *wall modes* characterized by a high wave number m and confined to the periphery $\rho \sim R$ of the domain [e.g., $\varepsilon_3 \approx 2.92 \times 10^{-4}$ at $R = 14$ and $\varepsilon_1 \approx 8.6 \times 10^{-5}$ at $R = 15$, Figs. 3(a) and (b)]. The

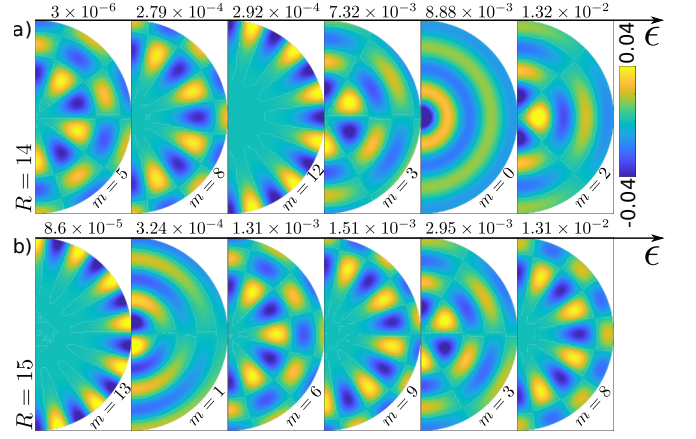


FIG. 3. The first six eigenfunctions on the half-disk predicted by linear stability analysis of the $u = 0$ state when (a) $R = 14$ and (b) $R = 15$. The eigenfunctions are sorted according to the eigenvalues ε . In each case, ε and the corresponding azimuthal number m are specified.

organization, stability and interconnections among the solution branches spawned by these modes, radial and wall, are discussed in the following sections. We start with these modes because (a) the radial mode is essentially 1D and, on the infinite disk and for the quadratic-cubic case, has been studied before; (b) the daisy mode is expected to be associated with quasi-1D snaking of localized daisies. Additionally, both show interesting further bifurcations. These two states are thus a natural starting point for discussing the organization of the very rich solution structure that exists even on small to moderate size disks.

III. THE AXISYMMETRIC CASE

A. Boundary value formulation

The steady state problem for axisymmetric solutions $u = u(\rho)$, $\rho \in [0, R]$, with the boundary conditions (2) can be written as the nonautonomous 1D boundary value problem

$$v'_1 = v_3, \quad (12a)$$

$$v'_2 = v_4, \quad (12b)$$

$$v'_3 = v_2 - q^2 v_1 - \frac{v_3}{v_5}, \quad (12c)$$

$$v'_4 = \varepsilon v_1 + \nu v_1^3 - v_1^5 - q^2 v_2 - \frac{v_4}{v_5}, \quad (12d)$$

$$v'_5 = 1, \quad (12e)$$

where $v'_i = \frac{dv_i}{d\rho}$, $i = 1, \dots, 5$. The connection between the components of $\mathbf{v} \equiv (v_1, v_2, v_3, v_4, v_5)$ and u is as follows:

$$v_1 = u, \quad v_2 = (q^2 + \Delta)u, \quad v_3 = u'_1, \quad v_4 = u'_2, \quad v_5 = \rho.$$

The system (12) is not the only choice for studying steady axisymmetric solutions of Eq. (1) as a boundary value problem, and similar formulations have been used before to explore the quadratic-cubic SH model [20–22]. The advantage of (12) is that the boundary conditions (2) for the system on the disk yield the uncoupled boundary conditions

$$v_3|_{\rho=0,R} = 0 = \partial_\rho u|_{\rho=0,R} = \nabla u \cdot \hat{\rho}|_{\partial\Omega}, \quad (13a)$$

$$v_4|_{\rho=0,R} = 0 = \partial_\rho(q^2 u + \Delta u)|_{\rho=0,R} = \nabla(\Delta u) \cdot \hat{\rho}|_{\partial\Omega}, \quad (13b)$$

$$v_5|_{\rho=0} = 0 = \rho|_{\rho=0}, \quad (13c)$$

which allow a simple numerical implementation, for instance, using the boundary value routine of **AUTO**, even for large R . This approach does not provide linear stability information, however, unless one solves the linearized problem in parallel (see e.g., [29–32]).

Since we are also interested in continuation of the branches that bifurcate from axisymmetric states, we also compute such states in 2D (albeit for moderate R) using **pde2path**, which yields linear stability information without additional effort.

B. Axisymmetric solutions on a small disk

We begin by demonstrating the equivalence between the **AUTO** solution of the 1D boundary value problem (12) and the **pde2path** solution of the 2D problem (1). In Fig. 4 we compare the *spot* and *target* patterns computed by both procedures when $R = 14$, $\nu = 2$, $q = 1$. Panel (a) shows the branch of axisymmetric solutions emerging from the trivial branch $u = 0$ at $\varepsilon = \varepsilon_5$ in the 1D and 2D formulations. To present the solution branches we employ the quasi-1D norm

$$\|u\|_* = \sqrt{\frac{1}{R} \int_0^R u^2(\rho) d\rho}. \quad (14)$$

This norm is preferred since it avoids suppressing *spots* at the center of the disk, in contrast to the 2D L^2 norm used later for nonaxisymmetric states. Panel (b) shows the radial profiles of two representative axisymmetric solutions at locations indicated by a circle and a star in the bifurcation diagrams in (a). These correspond to a spot and a target state, respectively. Because of the symmetry $u \rightarrow -u$ of the cubic-quintic SH equation, there is only one type of spot in this system, in contrast to the quadratic-cubic SH equation [21].

In contrast to the 1D problem on the real line [23], in the axisymmetric case described by (12) the $u = 0$ branch becomes unstable to an already localized state given by a Bessel function of the first kind of index zero. This is a consequence of the linear analysis in Section II A and is therefore the same regardless of the nonlinearity in (1). Continuation of this localized state produces characteristic snaking behavior [Fig. 4], qualitatively similar to that

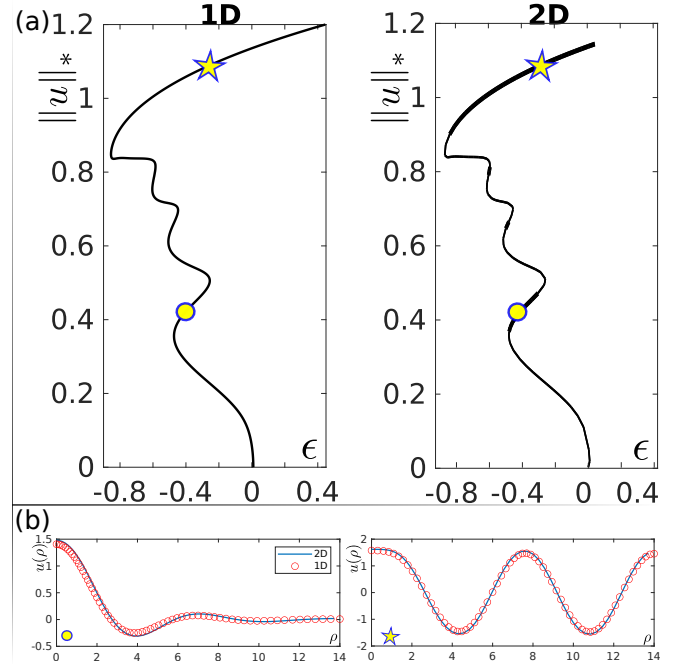


FIG. 4. (a) Comparison between the 1D (**AUTO**, left) and 2D (**pde2path**, right) continuation of axisymmetric states on a disk of radius $R = 14$ when $\nu = 2$ and $q = 1$. Thick line segments in the 2D case indicate stable solutions. (b) Radial profiles of representative spot and target states at locations indicated in (a) by an open circle and a star. Open red circles correspond to 1D computations while the solid blue line shows the corresponding profile obtained from 2D computations.

present in the quadratic-cubic case [20, 21]. We therefore refer to this branch as the *spot* branch. As one follows this branch, a half-wavelength is added to the spot solution after every other saddle-node and the solution thereby grows in spatial extent until it fills the domain, becoming a *target* state [Fig. 1(b)]. Using **pde2path** over the disk we computed in parallel the linear stability of the solutions along this branch, with stable (unstable) segments of the branch indicated by thick (thin) lines [Fig. 4(b)]. The result shows that most of the localized states on this branch are unstable, except for short segments after every fold on the left. Stable large amplitude domain-filling *target* states acquire stability shortly after the leftmost fold.

The transitions just described, namely the continuous evolution from the primary bifurcation into a spatially localized snaking structure, followed by a continuous transition into a domain-filling state, is characteristic of systems with nonstandard boundary conditions, as explained in [33]; in problems with Neumann or periodic boundary conditions, such as the SH equation on a periodic interval, the localized solutions appear in a secondary bifurcation from a periodic state that occurs at small amplitude, and these localized states reconnect to the domain-filling state near the fold of the latter. Thus

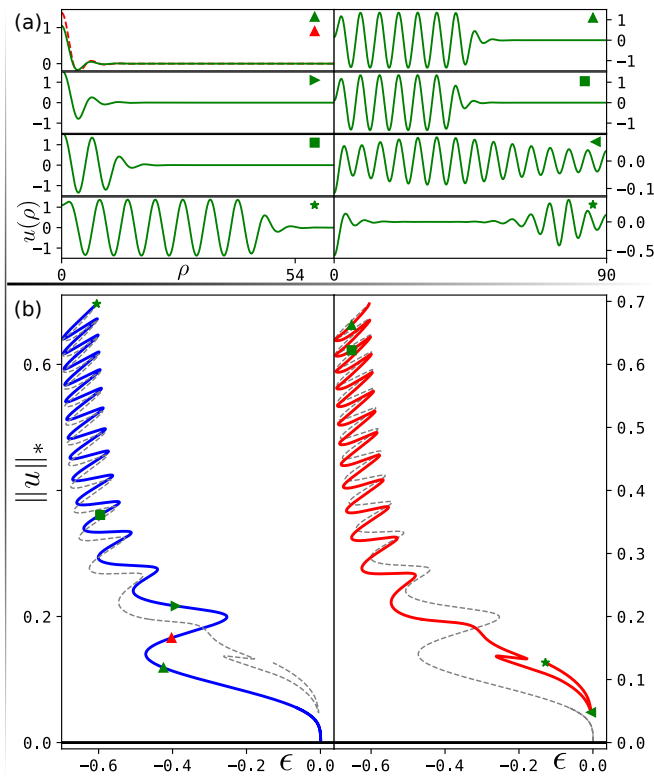


FIG. 5. Solution branch for the boundary value problem (12) on a disk of radius $R = 90$ when $\nu = 2$, $q = 1$ (b). *Spot* solutions are represented in blue (left) and evolve into *ring* solutions in red (right). The trivial solution $u = 0$ is in black. Each segment of the bifurcation diagram is accompanied by representative solutions (a) shown at locations indicated by different symbols (triangles, squares and stars).

the transition to and from localized structures takes place via bifurcations involving the periodic state, and does not occur smoothly following a single branch. In the present problem this departure from the periodic case is a consequence of the nonautonomous nature of the radial problem and not the boundary conditions.

C. Axisymmetric solutions on a large disk

Previous studies of axisymmetric solutions of the SH equation with a quadratic-cubic nonlinearity assumed an infinitely large ($R \rightarrow \infty$) disk [20–22]. In order to illustrate the similarities and differences between these studies and the cubic-quintic case studied here, we perform numerical continuation of (12) on a disk large enough ($R = 90$) to admit approximately 30 wavelengths across a diameter. The results are summarized in Figs. 5 and 6.

As in the case with $R = 14$ (Fig. 4), the branch of localized states for $R = 90$ bifurcates from $u = 0$ at $\varepsilon \approx 0$ as a spot solution, undergoes a series of folds, adding a

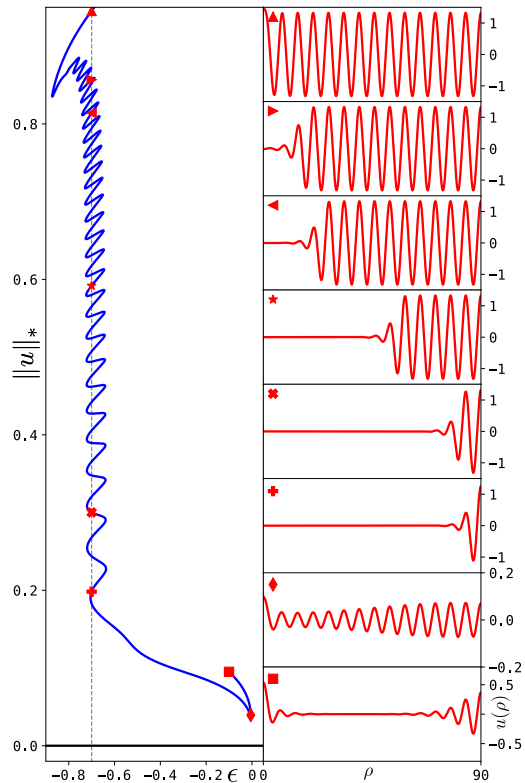


FIG. 6. Disconnected branch of solutions evolving from a target state for the boundary value problem (12) when $R = 90$, $\nu = 2$, $q = 1$ (left, blue curve). The trivial solution $u = 0$ is in black. Different symbols (square, diamond, star, crosses and triangles) mark the location of representative solutions (most along the dashed line $\varepsilon = -0.7$), illustrated on the right.

half-wavelength to the solution after every other fold as in the unbounded case [21] or the 1D cubic-quintic SH equation [23]. However, in contrast with the case $R = 14$, the branch eventually ceases to add more oscillations and instead starts to lose them. Figure 5(b) shows two copies of this branch; the left and right panels highlight the portions of the branch where the solution adds oscillations (blue) and loses oscillations (red).

Figure 5(b, left panel), shows that the process of adding oscillations to the spot solution continues for a number of folds, but instead of connecting to the target solution, there is now a transition where the solution changes from having a maximum at the origin (spot) to a local minimum (ring) [green star in (a)]. Further continuation of the branch [Fig. 5(b, right panel)] leads to a progressive loss of oscillations by the same mechanism, thereby reversing the process described above. This contraction process continues until the ring solution has only one maximum and one minimum. Subsequently the solution branch connects to a right-most fold located at $\varepsilon \approx 0$ (left-pointing triangle), corresponding to a small amplitude spatially modulated periodic state. Further contin-

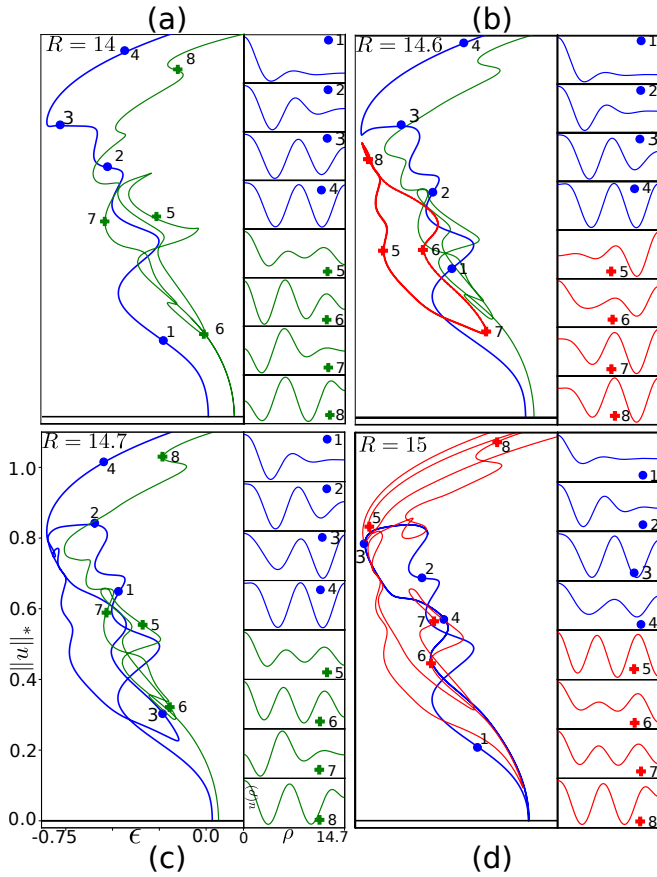


FIG. 7. Bifurcation diagram for axisymmetric states when (a) $R = 14$, (b) $R = 14.6$, (c) $R = 14.7$, and (d) $R = 15$ illustrating the pair of disconnections that are responsible for transforming the structure of (a) into (d). Sample radial profiles, at locations indicated by symbols (blue disks or red crosses), are included alongside.

uation of the solution past this fold results in states with an additional ring-like structure near the wall at $\rho = R$. This state, indicated by a star symbol in Fig. 5(b, right panel), is thus a combination of a spot at the origin and a ring-like structure along the wall. Like the states centered on $\rho = 0$, these wall structures are of two types, distinguished by whether they peak at the wall (a *wall spot*) or near the wall (a *wall ring*). Further continuation leads to further snaking of these combination states, either gaining or losing maxima, and eventually passing through a fold and turning into a yet different combination state (not shown) in a process that does not appear to terminate. The exact details depend strongly on the size of the disk, much as found in the 1D problem with Robin boundary conditions [34] and have not been studied in detail.

In contrast with the *spot to ring* transition described above, the existence of the *target* solution is independent of the radius of the disk. Figure 6 shows a target solution for $R = 90$ (see the up-pointing triangle in inset) and its

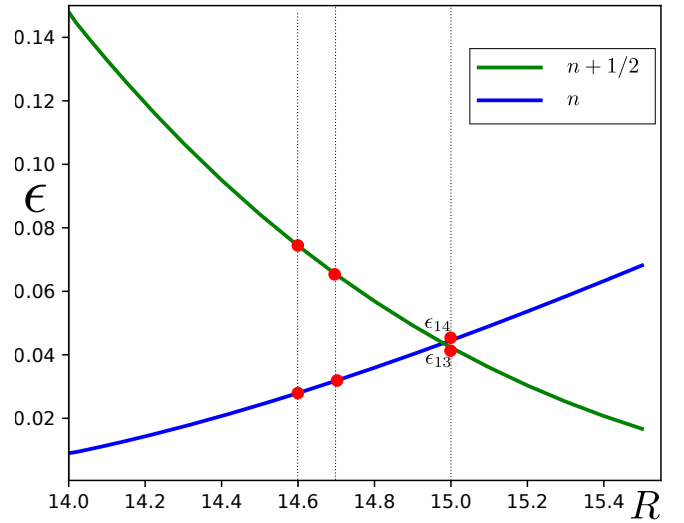


FIG. 8. Mode crossing in the linear stability problem (7) as a function of the radius R when $q = 1$. A marginal mode with n wavelengths (blue) is superseded by a marginal mode with $n + (1/2)$ wavelengths (green) at $R \approx 14.98$. Here $n = 2$. The eigenvalues ϵ_{13} and ϵ_{14} at $R = 15$ are indicated with red dots as are the corresponding eigenvalues at $R = 14.6$ and 14.7 , the radii employed in Fig. 7.

connection to the *wall spot* solutions (e.g., right-pointing triangle in inset). Further continuation of the branch leads to wavelength loss, much as observed after the transition from spot to ring [Fig. 5(b, right panel)]. The different insets illustrate this process (left-pointing triangle, star, and crosses). The wall-spot solution reaches a single maximum close to the prominent fold at $\epsilon \approx 0$ (diamond in inset) heralding a transition to a new combination state, consisting of a wall spot at $\rho = R$ and a spot at the center of the domain, $\rho = 0$. As far as we can tell both branches (that bifurcating from $u = 0$ and the continuation of the target branch) execute similar repeated upward and downward snaking but never connect, i.e., the target state remains disconnected from $u = 0$.

To understand this disconnection process we return in Fig. 7 to the moderate R case and discuss the transition from $R = 14$ (direct connection of the primary $u = 0$ branch to the target) to $R = 15$ (no such connection) in greater detail. Specifically, the figure shows the bifurcation diagrams for $R = 14$, $R = 14.6$, $R = 14.7$ and $R = 15$ together with sample solutions. The plot at $R = 14$ includes the second branch of axisymmetric states (green curve) that bifurcates from $\epsilon \approx 0.148$, in addition to the first branch (blue) that arises already at ϵ_5 . At this value of R these two branches are distinct [Fig. 7(a)] but this situation changes as R increases. At $R = 14.6$ [Fig. 7(b)] the spot state is still connected to the large amplitude target state although we are beginning to see a cusp-like feature in place of the leftmost fold on the blue branch. In addition, we have found a branch of axisym-

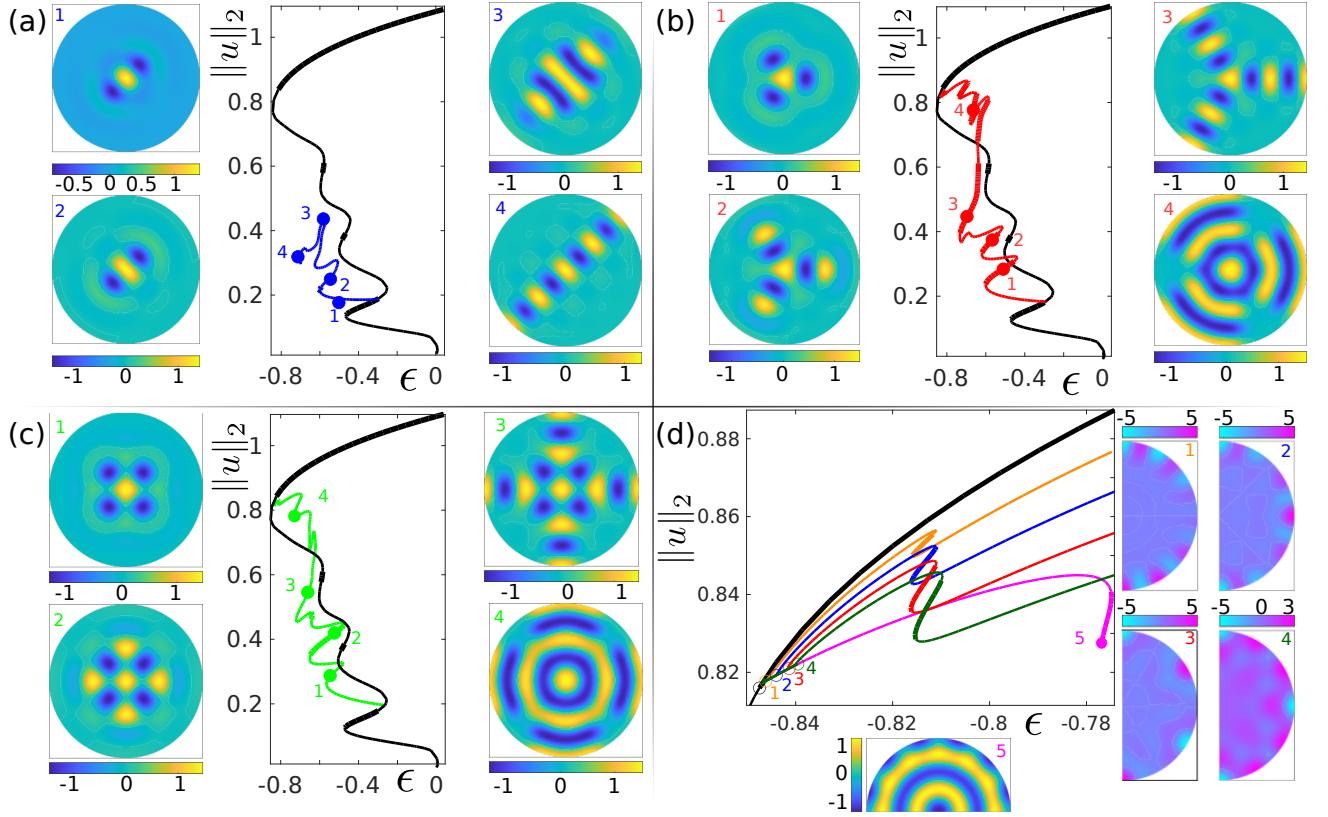


FIG. 9. Branches of multiarm solutions for $R = 14$, $\nu = 2$, $q = 1$. (a)–(c) $m = 2, 3, 4$ branches bifurcating from an axisymmetric spot at low $\|u\|_2$. Stability with respect to perturbations on the full disk is indicated by thick line segments. In each case, illustrative solutions are numbered and shown in corresponding insets. (d) Zoom of the bifurcation diagram with the $m = 12$ crown branch (magenta) and the branches of 1-arm (orange), 2-arm (blue), 3-arm (red), and 4-arm (green) states that bifurcate from it; the $m = 3, 4$ -arm states connect to the corresponding branches in panels (b) and (c). The four critical eigenfunctions on the $m = 12$ crown branch are shown alongside, together with the solution profile at location 5 on this branch. See Fig. 10 for further continuation and sample profiles along the $m = 1, 2$ branches bifurcating from the first two bifurcation points on the crown branch.

metric states lying on an isola (red curve). Such isolas of spatially extended states are present even in the 1D cubic-quintic SH equation [35]. This isola also possesses a cusp-like feature in the vicinity of the cusp on the spot branch indicating that a codimension-two reconnection is about to happen. Figure 7(c) for $R = 14.7$ describes the situation after this reconnection. The spot branch (blue) remains connected to the target states but now incorporates the isola states in the process. State 4 on the first target branch differs from state 8 on the second target branch by approximately half a wavelength, as expected of solutions connected via a fold.

A further transition occurs by $R = 15$ [Fig. 7(d)]. Figure 7(c) shows that the leftmost fold on the second spot branch (green) is approaching close to the first branch (blue) at $\epsilon \approx -0.76$ and amplitude $\|u\|_* \approx 0.76$, suggesting that a further reconnection takes place. This is indeed the case and Fig. 7(d) shows that as a result the blue branch becomes disconnected from the target states, and instead connects back to $u = 0$ at ϵ_{14} , i.e. at the origin of the second spot branch. The proximity of ϵ_{13} and ϵ_{14} at this value of R is responsible for the appearance of

the cusp-like feature at $u = 0$ in the blue branch seen in the figure. Moreover, the target states on both the blue (profile 4) and green (profile 8) branches in Fig. 7(c) are now connected. These are part of a sequence of small and large amplitude states that are disconnected from $u = 0$ and shown in red. These may form via the incorporation of additional isolas into the branch. In fact, at $R = 15$ the target states are part of a heavily folded upper branch responsible for the appearance of additional target states at large amplitude.

Evidently, the transition that leads to the break up of the branch connecting the first spot branch to the corresponding target states is exceedingly complex. In fact, we expect that the transition shown in Fig. 7 is one of many such transitions. This is because the system has a preferred radial wavelength. As a result, as R increases, the system must repeatedly execute disconnections of this type, in order that the new lowest radial mode is again able to connect to the target state with the correct number of wavelengths. These transitions are triggered linearly when successive bifurcation points on $u = 0$ pass through one another as R increases (Fig. 8), and these

are inevitably associated with additional nonlinear transitions of the type shown in Fig. 7. Similar behavior occurs in 1D as well [36].

IV. NONAXISYMMETRIC SOLUTIONS ON A DISK

A. Multiarm states

We now explore secondary bifurcations from axisymmetric states to nonaxisymmetric structures. For this 2D problem we use `pde2path` on the half disk of radius $R = 14$ but compute the stability of the solutions on the whole disk. The results are presented using the 2D L^2 norm

$$\|u\|_2 = \sqrt{\frac{1}{|\Omega|} \int_{\Omega} u^2(\mathbf{x}) \, d\mathbf{x}}, \quad (15)$$

with ε as the continuation parameter unless otherwise stated. The results are summarized in Fig. 9.

For $R = 14$, the $m = 2$ mode is the first nonaxisymmetric mode that bifurcates from the axisymmetric state with a spot at the center of the domain [Fig. 9(a)]. The bifurcation is characterized by the appearance of new maxima on opposite sides of the spot (state 1). The resulting branch snakes, a behavior that is associated with the successive nucleation of additional maxima at the tips of the resulting arms after every second fold (states 2 and 3), in a process that resembles the growth of localized structures in the 1D cubic-quintic SH equation. However, in contrast to the 1D SH equation, as this is taking place the structure broadens into a *worm* [37] prior to reaching the boundary at $\rho = R$ and refocusing (state 4). In addition, further continuation of the $m = 2$ branch did not lead to lateral broadening of the arms and the branch does not approach a domain-filling target state, in contrast to the cases $m = 3, 4$ discussed next. Instead the $m = 2$ arms retract towards the boundary forming a pair of spots at opposite ends of a diameter (not shown).

We next discuss the $m = 3$ [panel (b)] and $m = 4$ [panel (c)] branches. These consist of 3-arm and 4-arm states, respectively. Like the $m = 2$ branch, these branches start at low norm on the branch of axisymmetric states (state 1), and grow by essentially the same snaking process as the $m = 2$ branch until they reach the boundary. However, at this point snaking gives way to a 'vertical' increase in the norm that is associated with rapid lateral expansion of the arms. This type of growth is not associated with snaking because of the absence of pinning in this direction [37] and takes place in the vicinity of the Maxwell point, i.e., the ε -value at which the energy $\mathcal{F}[u]$ of the target state vanishes. This lateral expansion generates states that almost completely fill the domain, leaving 3 (resp. 4) radial gaps or holes. The snaking observed at the top of this interval of rapid expansion is associated with the successive formation of complete rings around

the disk center, i.e., with the gradual retraction of the radial holes towards the boundary.

Surprisingly, we find that neither state connects to a domain-filling target state. Instead, this connection takes place via a new, intermediate state we refer to as a *crown* state. This state bifurcates from the target branch at the point where the target branch stabilizes, and represents a near-axisymmetric state with an $m = 12$ modulation superposed on the stripe adjacent to the wall (magenta branch in panel (d) and sample plot 5). The right column in panel (d) shows the first 4 bifurcation directions along the magenta branch. These correspond to the appearance of 1, 2, 3 and 4 equispaced holes along the wall, and we find that the $m = 3, 4$ branches in panels (b,c) terminate on the $m = 12$ crown branch at the corresponding $m = 3, 4$ bifurcations (red and green branches). Thus, contrary to expectation, none of these states connect directly to the target state.

The 1-arm (orange) and 2-arm (blue) hole states that bifurcate from the magenta branch in panel (d) have been continued away from the crown branch and the results are illustrated in Fig. 10. Both branches extend to low norm and do so via rapid broadening of the hole that turns the hole into a 1-arm (resp. 2-arm) state. However, neither branch connects to the branch of axisymmetric spots. Instead, the 1-arm state gradually retracts towards the boundary via snaking and turns into a wall-attached spot (state 4 in panel (a)). The 2-arm state likewise shrinks into a pair of spots on the boundary (state 4 in panel (b)). In both cases these spots subsequently regrow new spots towards the interior, but no longer along the radius (not shown).

In summary, for $m = 3, 4$ we have a connection between the radial spot at low norm and the $m = 12$ crown branch very close to the top left fold on the target branch. For $m = 2$ we have two disconnected branches of 2-arm states, one emerging from a small amplitude spot, and the other from the $m = 12$ crown branch at the top, both exhibiting very similar 2-arm states in between, for $\|u\|_2 \approx 0.4$, say, but the two branches do not connect. For $m = 1$ we only have one branch, with no bifurcation to a 1-arm state from an axisymmetric spot at low $\|u\|_2$. Remarkably, all of these m -arm branches include some stable states.

The $m = 1, 2, 3, 4$ -arm states computed above are invariant under rotations $\phi \rightarrow \phi + 2\pi/m$ and reflections across a suitable line. These operations generate the group D_m and our continuation procedure respects this symmetry, unless tertiary bifurcations take place that break it. D_m -symmetric states may also bifurcate directly from the trivial state, see, for instance, the 2nd, 3rd and 6th mode in Fig. 3(a). In addition, branches of D_m^- -symmetric states are also present; these states change sign upon rotation by $2\pi/m$. In Figs. 11(a) and (b) we show two such states, with symmetry D_4^- and D_6^- , respectively. These states are D_2 and D_3 -invariant but not D_4 and D_6 -invariant.

Like the multiarm solutions of Fig. 9 and Fig. 10, the

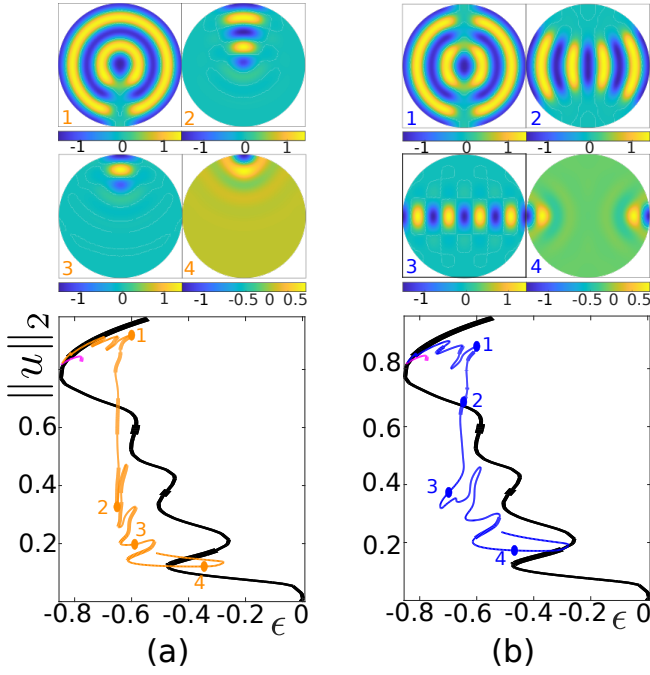


FIG. 10. Continuation of Fig. 9 showing the $m = 1, 2$ branches from their origin on the $m = 12$ crown branch. Stability with respect to perturbations on the full disk is indicated by thick line segments.

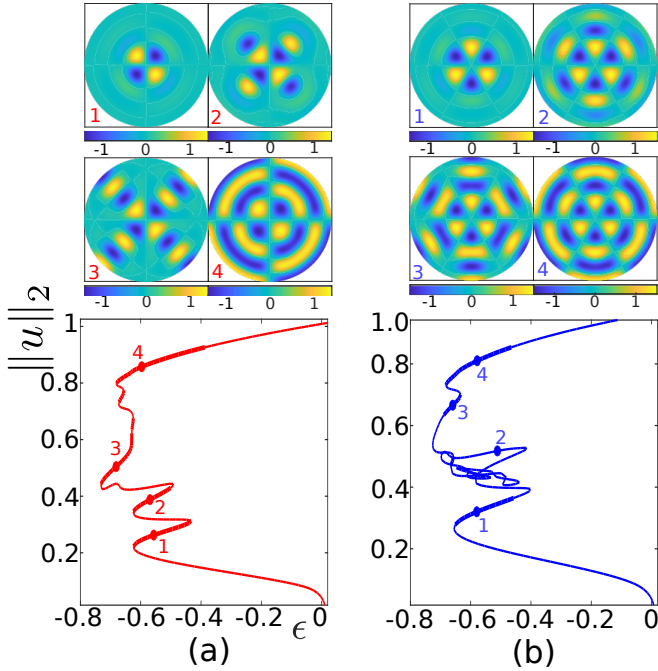


FIG. 11. Branches of solutions with the symmetry D_m^- emerging from bifurcations of the trivial state $u = 0$. Panels (a) and (b) show the 4^- and 6^- -arm states, respectively. The bottom panels show the corresponding bifurcation diagrams in red and blue. Sample states at locations indicated by filled dots are shown in the top panels. Stability with respect to perturbations on the full disk is indicated by thick line segments.

D_m^- states start as localized structures near the center of the domain but develop m arms as one proceeds to larger amplitude which broaden into extended D_m^- target states after reaching the wall (insets 1-3 in each case). Because of the D_m^- symmetry these states fill the domain with a target-like structure consisting of $2\pi/m$ slices of the disk with the same pattern but alternating sign (see inset 4 in each case). The D_m^- symmetry is present in the problem because of the $u \rightarrow -u$ symmetry of the cubic-quintic SH equation. Mathematically, the same symmetry is present in porous media convection and it therefore comes as no surprise that states similar to the $m = 4$ states in Fig. 9(c) were found in numerical continuation of the relevant equations of fluid dynamics on a periodic domain with a square cross-section [38, 39]. In particular, in this problem one finds both D_4 and D_4^- -symmetric structures. However, because of the periodicity of the spatial domain, these states bifurcate from a branch of periodic structures rather than directly from the trivial state.

B. Daisy states and their bifurcations

Our next family of nonaxisymmetric states is characterized by high azimuthal wave number. For this reason these states are localized towards the periphery of the domain, i.e. they are wall modes. Following [40] we refer to them as daisy states. Figure 1(g) shows an example for $R = 14$ and $\nu = 1.5$. The daisies are periodic in the angle ϕ and have symmetry D_m , $m \gg 1$. Consequently they are easily computed on smaller sectorial domains with opening angle $2\pi/m$ or even π/m ; in the latter case the solution will have the property $u(\rho, \pi/m) = -u(\rho, 0)$ for all ρ , with $u_\phi(\rho, \pi/m) = u_\phi(\rho, 0) = 0$, modulo rotations of the state.

The blue branch in Fig. 12 represents the computed daisy states, with sample states at locations **wu** and **wd** shown in the top panels. The daisy states bifurcate subcritically from the trivial state $u = 0$ at ϵ_3 and acquire linear stability beyond the left fold of the blue branch, although they lose it again at yet larger amplitude, see Fig. 13 and Fig. 18 below for details. As before, the notion of stability always refers to stability with respect to perturbations on the whole disk, even for solutions computed on smaller sectors. Since the daisies represent subcritical periodic states, we expect to find, by analogy with the 1D cubic-quintic SH equation [23], localized wall states resembling a partially plucked daisy in appropriate parameter regimes. We further expect snaking branches of such plucked daisies where petals are added/removed after every other fold. To obtain these states we start with a moderate subcriticality, $\nu = 1.4$, and discuss how the scenario changes for stronger subcriticality, namely $\nu = 1.5$. In Fig. 12 we show branches of localized daisies of odd (green) and even (red) parity; sample states are shown in the panels on the right of the figure, together with 1D profiles along their periphery. These illustrate

the analogy between these states and the 1D SH scenario of [23]. As in the 1D SH case, the odd and even branches of localized daisy states are connected via rung states, shown in black and in the inset labeled **r**. There are in fact four such branches owing to the symmetry $u \rightarrow -u$. These localized daisies bifurcate from the daisy branch at small amplitude (bottom right corner of the bifurcation diagram in Fig. 12), undergo snaking whereby the solution adds half a wavelength at either end after every left fold, eventually leaving just one plucked petal of the daisy, before terminating on the complete daisy state near its fold, likely via Eckhaus instability, cf. [36]. In addition to the even and odd branches of localized states shown in Fig. 12, we also found 2-pulse localized daisies (magenta branch in Fig. 13(a) as well as 3- or more-pulse states (not shown) all of which that behave similarly to the 1-pulse case.

The above 2-pulse states lie on a continuous branch that snakes just like the 1-pulse branch but bifurcates from the daisy state at larger amplitude than the 1-pulse branch, and likewise terminates on this branch farther from its fold. This is because the computed 2-pulse states are equidistant and so behave like 1-pulse states on the half-domain. We conjecture that non-equispaced 2-pulse states lie on isolas, like the corresponding states in the 1D SH equation [41], but have not computed such states.

It turns out that the daisy snaking scenario in Fig. 12 depends rather strongly on ν . In Fig. 13(a) we again show the daisy branch at $\nu = 1.4$ in blue, the branch of even 1-pulse states in green and even 2-pulse states in magenta, and number representative folds 1–4. Panels (b) and (c) show the continuation of these folds in the (ν, ε) plane. In the 2-pulse case the fold extends beyond $\nu = 1.5$ but retreats at larger ν , yielding two possible solutions at $\nu = 1.5$ [magenta triangles, panel (d)]. In the 1-pulse case, folds 1 and 3 exist at $\nu = 1.5$ (and beyond), whereas fold 2 [in blue, panel (b)] turns back before $\nu = 1.5$.

Using the solutions at $\nu = 1.5$ [vertical dashed line in Figs. 13(b) and (c)] as starting points, we return in Fig. 14 to one-parameter continuation. Keeping $\nu = 1.5$ fixed and continuing the 2-pulse state both up and down in amplitude (green and brown curves, respectively) yields the complete snaking branch of even states of this type. [Fig. 14(b)]. This branch connects with the daisy branch at the top and bottom. We can also perform one-parameter continuation of the 2-pulse state in ν , leading to the isola shown in Fig. 14(a). Profiles 1–2 show that the states on this isola correspond to a localized daisy whose petals at $\phi \approx 0$ are beginning to expand into the interior of the disk.

Since fold 2 of the 1-pulse branch does not exist at $\nu = 1.5$ [Fig. 13(a) and (b)], we expect to see a disconnection of folds 1 and 3 when performing continuation in ε . This is illustrated in Figs. 14(c) and (d). The upper fold 3 from Fig. 13(a) connects to the daisy branch near its fold [green segment in Fig. 14(d)], and continuation in the opposite direction yields snake-like behavior

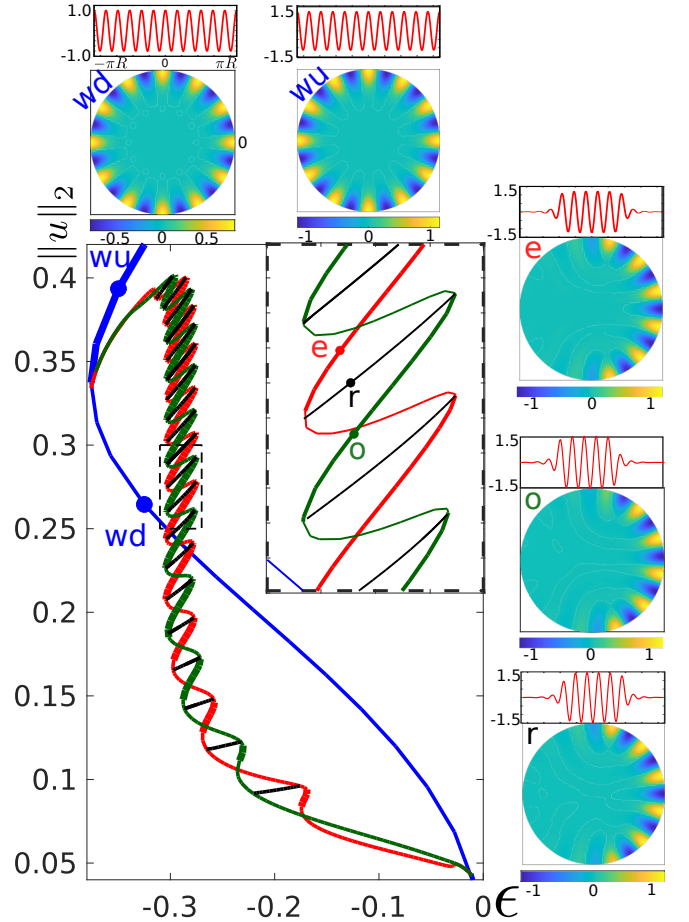


FIG. 12. The wall modes or daisy states (blue) and their secondary bifurcations computed from Eq. (1) when $R = 14$, $\nu = 1.4$, and $q = 1$. The secondary branches of (e)ven (red) and (o)dd (green) localized states are connected via (r)ung states (black). A zoom of the bifurcation diagram provides more detail of the localized branches. Representative solutions marked with dots in the bifurcation diagram are represented in the respective insets. The 1D profiles correspond to each solution along its periphery.

[brown segment in Fig. 14(d)] until some of the petals of the solution grow towards the interior of the disk, forming worm-like structures. Similarly, the lower fold 1 from Fig. 13(a) connects to the daisy branch near the bottom, and continuation in the opposite direction also leads to snaking followed by the development of worm-like structures [Fig. 14(c)]. In both cases the continuation was stopped at an arbitrary point for the sake of clarity. The 2-pulse snaking branch likewise breaks at $\nu \approx 1.535$ when fold 4 in Fig. 13(a) disappears [Fig. 13(c)].

In contrast with the 1D case, here the extra degree of freedom in the radial direction leads to fat wall-attached worms confined to part of the full disk. As a result, the branch of localized daisy states is no longer able to terminate on the daisy branch and we have been unable to determine its ultimate fate. We note that fat worm-like

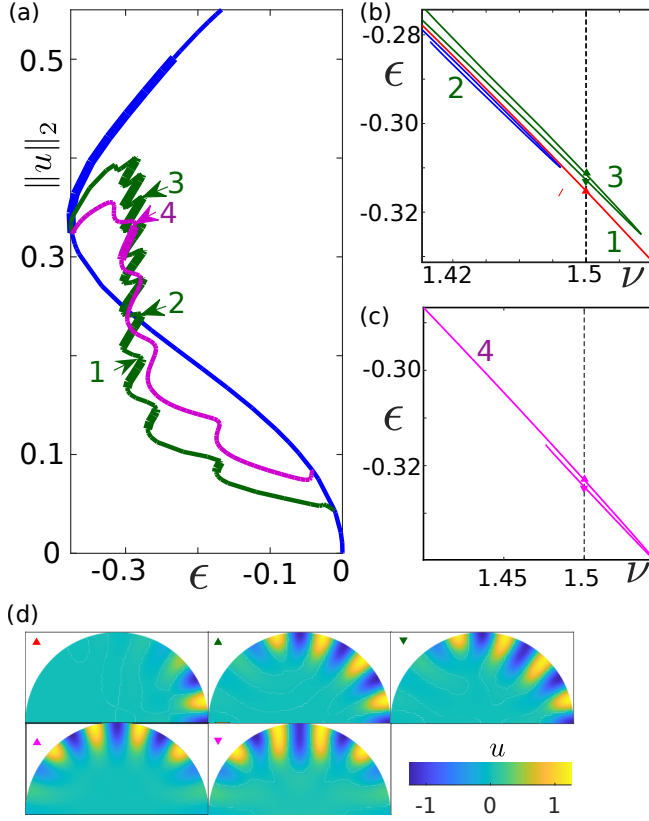


FIG. 13. Branches of one- and two-pulse solutions on the half-disk for the case $R = 14, q = 1$, together with continuation of selected folds in ν . (a) Bifurcation diagram of the daisy branch (blue), together with the branches of 1-pulse (green) and 2-pulse (magenta) localized daisy states when $\nu = 1.4$, with four representative folds numbered 1–4. (b) Continuation of folds 1–3 on the 1-pulse branch in the (ν, ϵ) plane. The numbers next to each curve correspond to the folds in (a); states at $\nu = 1.5$ are marked by triangles. (c) Same as (b) for the 2-pulse folds. (d) Five representative solutions from (b) and (c).

states are well-known solutions of the SH equation in the plane, and these may be held together both by curvature of the boundary and by pinning due a wave number gradient normal to the boundary [37]; in other cases these states are unstable leading to temporal growth [42]. We associate the appearance of the fat worms with the initiation of the filling transition, whereby the disk gradually fills with an extended stripe state as parameters change. Evidently this transition occurs as a result of the advance of the front connecting the wall-attached stripe state to the trivial state, towards the origin of the disk. How the location and shape of this front depend on parameters is an important question; dynamical integration suggests that outside the snaking region the worm state either collapses (to the left of the snaking region) or else grows dynamically leading to dynamic filling of the domain interior (to the right of the snaking region). See Sec. VI for further discussion.

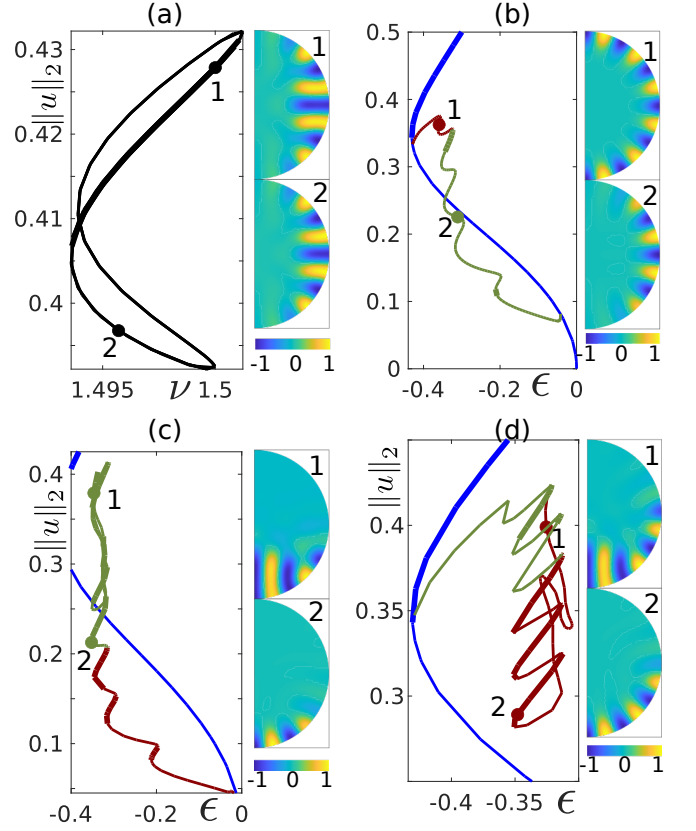


FIG. 14. Continuation of representative states in Fig. 13(d) in the parameter (a) ν , starting from the downwards pink triangle, (b) ϵ , starting from the upwards pink triangle, (c) ϵ , starting from the red upwards triangle, and (d) ϵ , starting from the upwards green triangle. In (b)–(d), green (red) correspond to continuation for increasing (decreasing) ϵ . Profiles with representative solutions are included.

V. ENERGY OF SOLUTIONS

Since the SH equation seeks to minimize the free energy (5), the global energy minimum is of particular interest. In this section we therefore compare the energies of the previously obtained solutions, restricting the discussion to the parameter regime $R = 14, q = 1$, and treat the cases $\nu = 2$ (Figs. 15 and 16) and $\nu = 1.4$ (Fig. 17) separately, aiming to identify the branches with the lowest energy. In both cases we show the norm $\|u\|_2$ [Eq. (14)] and the corresponding energy \mathcal{F}/A [Eq. (5)] in the top and bottom panels, respectively. In the energy representation the folds in the former become cusps, making the branches hard to distinguish. Consequently, we have split the branches into different subfigures, and indicate some sample solutions (using a star or an arrow) in order to illustrate the mapping between these two representations. In all cases the energy vanishes close to the Maxwell point for the target state.

Figure 15 shows four branches emerging from the trivial state (green) when $\nu = 2$. Panel (a) compares the

axisymmetric (magenta) and daisy (brown) states. For small values of ε , the least energy state is the trivial state $u = 0$. At $\varepsilon \approx -0.63$, the energy of the axisymmetric states crosses zero becoming negative and the minimum energy state is a target state. For larger values of ε , the energy of the daisy states also becomes negative but remains larger than that of the target states.

The m^- -arm branches emerge from the trivial branch as localized solutions. Further continuation leads to a series of folds, filling the domain with a multiarm extended pattern with the symmetry D_m^- . Figure 15 shows the branches for $m = 4$ and $m = 6$ in black [panel (b)] and red [panel (c)], respectively. As the branch undergoes the above-mentioned series of folds, the free energy oscillates between adjacent cusps. Continuation of the branch in the direction of increasing norm leads to increasing energy until the solution reaches the fold at the top left of the bifurcation diagram in the top panels. Beyond this point, the energy decreases again and eventually becomes negative. This occurs first for $m = 4$ and then for $m = 6$. In both cases the energy is always greater than that of the target state at the same value of ε .

Figure 16 illustrates the energy of the secondary branches when $\nu = 2$, showing the branches of the 3^+ and 4^+ -arm solutions in panels (a) and (b) and the corresponding free energy in panels (d) and (e). The latter resemble the plots in Fig. 15. Panel (c) shows the fate of a localized daisy solution, after it emerges from the daisy branch. As discussed in Sec. IV B, the localized daisy states initially add new petals every other fold. In the present case the solution subsequently develops into a 1-worm-like structure instead of adding more petals, with the stripes extending farther and farther into the domain, eventually generating an Ω -shaped structure [panels (c) and (f)], in contrast to what happens in Fig. 18(b) below. Figure 16(f) shows that as the structure expands, energy starts to decrease and the Ω state (star, inset) that results has negative energy. At this value of ε , this is the solution with the smallest energy after the target state.

As shown in Sec. IV B, when $\nu = 1.4$, the localized daisy states instead exhibit snaking behavior analogous to the 1D SH equation [23], and this also holds for the energy. In Fig. 17 we show the even (red), odd (green) and equispaced two-pulse (yellow) branches of localized daisy states, with representative folds marked with arrows and numbered. In all cases, localized solutions with higher $\|u\|_2$ norm have lower energy. The rung states are not shown. The 2-pulse states always have greater energy than the odd and even single pulse states.

In summary, the energy provides the following description in terms of the lowest energy states: for small values of ε , the branch with the smallest energy is the trivial one. As ε increases, axisymmetric states become energetically more favorable. For yet larger values of ε , the energy of the 4^- and 6^- branches becomes negative as is the energy of the Ω state in Fig. 16(f) but these states never become global energy minima. In general spatially extended states have lower energy than localized states.

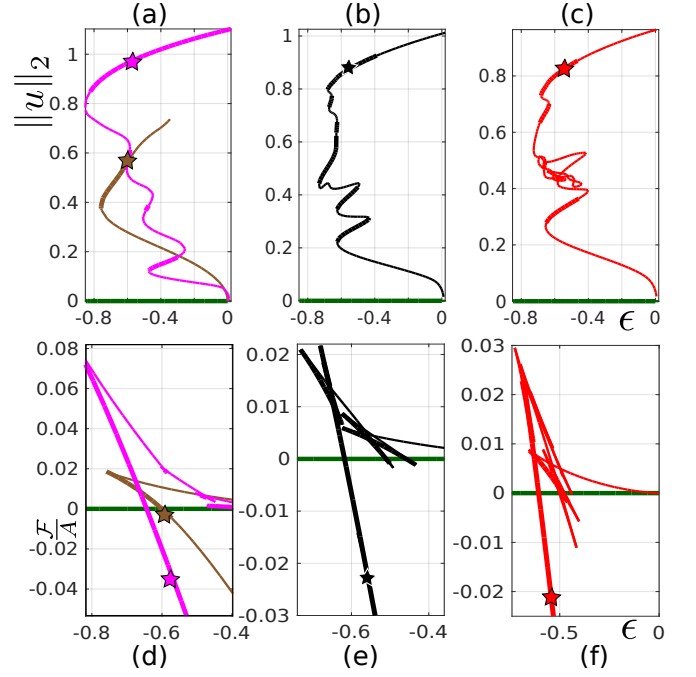


FIG. 15. Solutions for $\nu = 2$ as a function of ε shown in terms of (a)–(c) their norm $\|u\|_2$ (14) or (d)–(f) their energy (5) per unit area. The trivial branch is in green. Panel (a) compares the axisymmetric (magenta) and daisy (brown) states. Panels (b) and (c) show the 4^- -arm (black) and 6^- -arm (red) branches, respectively. In each case, sample points are marked with a star to illustrate the mapping between the norm and the energy \mathcal{F}/A . All computations are for a disk with $R = 14$, $q = 1$.

VI. FURTHER PATTERNS

We now briefly discuss some patterns to the right of the snaking region of the localized daisy states, and also perform some direct numerical simulations (DNS). The loss of stability of the daisy branches with increasing ε generically results in wall-attached worms, but the subsequent behavior is sensitive to the value of ν . In Fig. 18 we again contrast the cases $\nu = 1.4$ and $\nu = 2$ when $R = 14$. Panel (a), computed on the half disk for $\nu = 1.4$, shows that the first bifurcating branch (orange) contains states similar to those in Fig. 14, namely a stable wall-attached 3-worm which subsequently turns into a mix of wall-spots and interior spots, but does not become stable again. The next branch (green) bifurcates very close to the first, starts as a wall-attached 4-worm, and turns into a mix of stripes perpendicular to the wall with spots in between. Stable solutions exist up to $\varepsilon \approx -0.1$. Solution 4 is the result of DNS from state 3, just after its loss of stability, and yields vertical stripes near the disk center. Essentially the same states are obtained on the full disk, where DNS from unstable initial conditions generates various combinations of stripes near the center, depending on meshing details, or differences in initial perturbations.

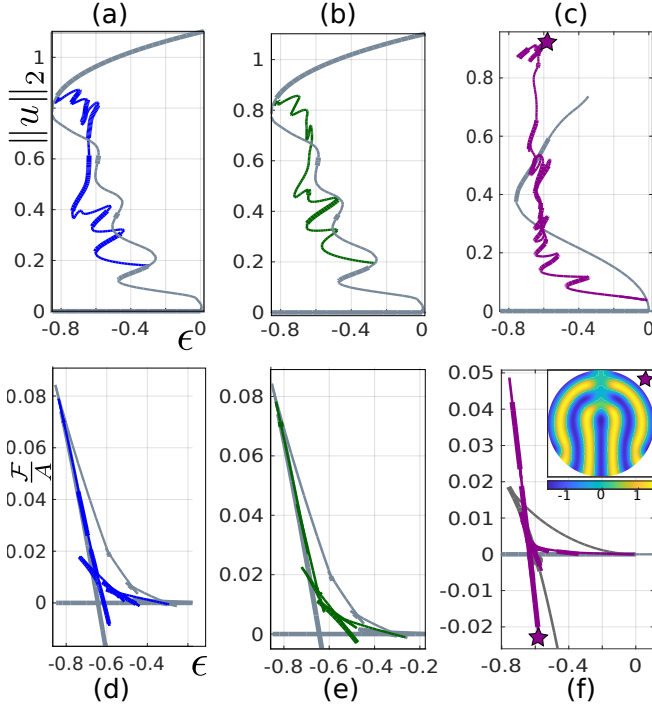


FIG. 16. Secondary bifurcations from (a), (b) the axisymmetric branches and (c) the daisy branch when $\nu = 2$, using the same convention as in Fig. 15. Blue and green branches represent the 3^+ and 4^+ -arm solutions, respectively. Panel (c) shows the branch of localized daisy states (purple) bifurcating from the daisy branch (gray). The branch initially snakes (localized daisy states) but subsequent continuation leads to a worm-like state and then to an Ω -shaped state (inset) as the stripes extend far into the domain (star).

For $\nu = 2$ [panel (b)], the first bifurcation is to a Z_4 -symmetric wall-attached 4-worm, which subsequently expands into the interior of the disk in the form of regular stripes but then breaks up, due to overcrowding, into a mix of spots and stripes, leaving a hole at the disk center. DNS from the Z_4 -symmetric state 3 yields state 4, where the Z_4 symmetry is lost when stripes recombine to fill the interior.

The target patterns and the m -arm states from Sec. III all consist of stripes parallel to the wall, while the daisies, localized daisies, and patterns 4 from Fig. 18(a) and (b) consist of stripes perpendicular to the wall. In contrast, the Ω pattern from Fig. 16(f) has both. Evidently, away from the stability regions of the patterns discussed so far, we may expect patterns of spots and stripes with some stripes parallel and others perpendicular to the wall. One example, shown in Fig. 19, is the result of DNS at $(\varepsilon, \nu, q) = (-0.6, 2, 1)$ starting at $t = 0$ with parallel stripes $(u_1(x, y), u_2(x, y)) = (\cos(4\pi y/14), 0)$ in terms of the 2-component second order system (A.1). The solution quickly converges to (the stable) state 1. On continuing the solution from location 1 to larger ε we find that the pattern remains stable for all ε values

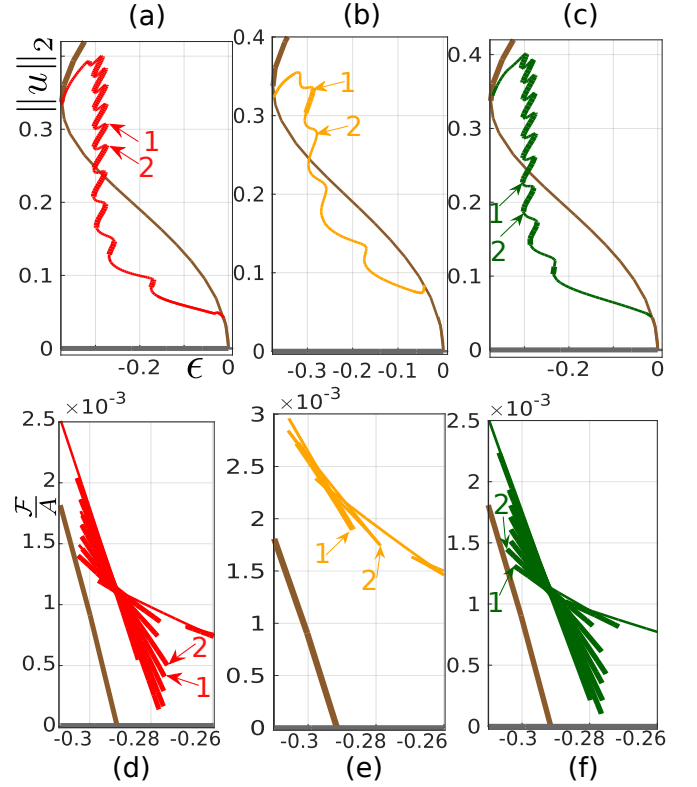


FIG. 17. Solutions for $\nu = 1.4$ using the same convention as in Fig. 15. The daisy branch is shown in brown with branches of even [red, panel (a)], odd [green, panel (c)] and equispaced 2-pulse [yellow, panel (b)] localized daisy solutions also shown. Representative folds of the localized branches are numbered to enable comparison with the energy plots in panels (d)–(f).

reached without a qualitative change of shape. Continuation to smaller ε yields the magenta branch, which initially shows some snaking whereby the top and bottom stripes disintegrate into spots. Shortly after state 3 the branch loses stability and never regains it; the disintegration (and partial recovery) of the stripes continues, however, but the branch apparently never connects to any of the states already discussed. Similar behavior is obtained for $\nu = 1.4$ and ε in the range -0.3 to -0.1 (not shown).

VII. DISCUSSION

We have explored numerically the variety of states described by the prototypical subcritical SH equation on a finite disk with Neumann boundary conditions. We have chosen the cubic-quintic case in order to eliminate the preference for hexagonal structures in, for example, the quadratic-cubic case. The key point about the SH equation is its characteristic scale $2\pi/q$. In the quadratic-cubic case, hexagonal structures on this scale are more easily accommodated within a disk of radius R than the

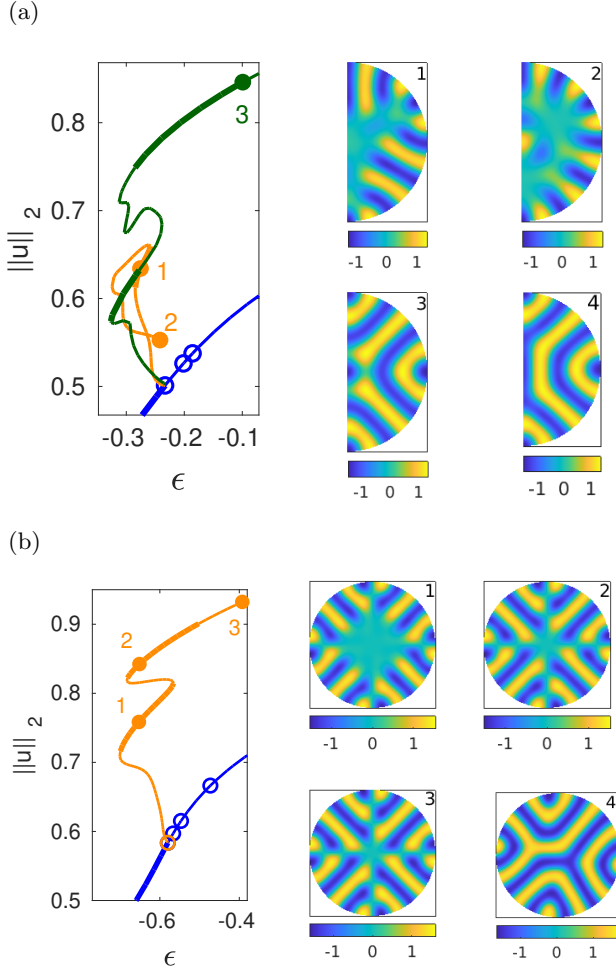


FIG. 18. Branches bifurcating from the daisy branch (blue) when it loses stability at large amplitude. (a) $\nu = 1.4$. The first bifurcating branch (orange) initially consists of stable wall-attached 3-worms, which disintegrate upon further continuation into various combinations of boundary and center spots but never again become stable. The next branch consists of wall-attached 4-worms (green) which turn into a combination of stripes perpendicular to the wall, spots in between, and a hole at the disk center, with intervals of stability up to $\epsilon \approx -0.1$. State 4 is generated from DNS starting from state 3, slightly to the right of the stability range of the green branch. (b) $\nu = 2$. The first bifurcating branch is now a snaking branch of wall-attached 4-worms similar to those in (a); state 4 is again obtained from DNS starting from state 3.

stripes that are preferred in the cubic-quintic case. Thus the latter is more interesting from a physics point of view, and the number of wavelengths $2\pi/q$ that can be accommodated along the diameter or the circumference of the disk becomes a key parameter. Throughout we focused on steady states since all time-asymptotic states of the model are necessarily steady.

Because the primary bifurcation in our model is subcritical we expect both spatially extended structures and spatially localized structures. We focused on relatively

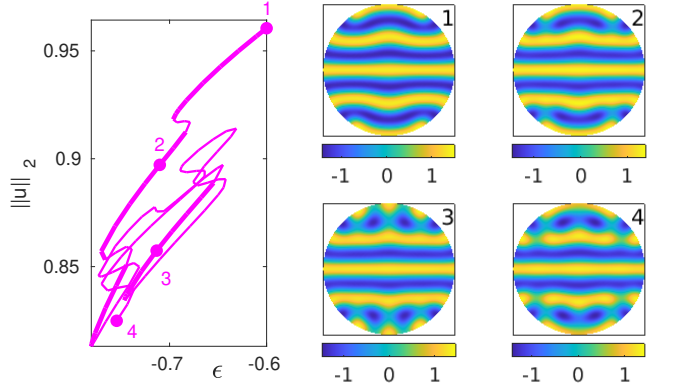


FIG. 19. Patterns for $\nu = 2$ obtained from DNS with straight horizontal stripes as initial condition (state 1), and subsequent continuation in ϵ .

small disks but even these already allow a large variety of (stable) patterns in the subcritical regime. Spatially extended states include target patterns consisting of concentric stripes parallel to the boundary and worm states with stripes normal to the boundary, while the localized structures can be divided into two types: those localized at the center of the domain and those localized at the boundary. States exhibiting some stripes that are normal to the boundary and others that are parallel to it, such as the Ω pattern in Fig. 16(f), have also been obtained. However, neither PanAm-type patterns with convex stripes whose curvature is not imposed by the boundary nor spirals [43] were found, suggesting that such states require large scale flows for their maintenance. Such flows are of course absent from the model studied here.

For axisymmetric states we also considered the case of large R . The states then either have a monotonically decaying envelope and are then referred to as *spots*, or one that peaks away from the center or boundary, in which case we refer to them as *rings*. We found that in relatively small disks the central spot exhibited typical snaking behavior as it grew in extent, eventually filling the domain and becoming a target state. In contrast, in larger disks the spot state undergoes a transition to a domain-filling ring-like state that subsequently breaks up into a pair of ring structures, one near the center and one near the outer boundary. As one follows the solution branch further the connection between these states repeatedly forms and breaks, leading to exceedingly complex behavior of the solution branch.

The axisymmetric states are subject to secondary symmetry-breaking bifurcations. We explored these on a relatively small disk, and identified secondary states with D_2 , D_3 and D_4 symmetry, representing states with 2, 3 and 4 arms that gradually extend in length while remaining laterally localized. Once the arms reach the boundary, they begin to spread laterally, terminating on a 'crown' state that bifurcates from a domain-filling tar-

get state close to its fold [Fig. 9(d)]. This is not the case, however, for primary D_m^- -symmetric states, for which rotations by $2\pi/m$ are equivalent to changing the sign of u (Fig. 11). These states exhibit similar growth behavior but cannot connect to a target state.

In addition we also studied subcritical azimuthally periodic wall states (daisies), and showed that these were accompanied by azimuthally localized daisy states. For weak to moderate subcriticality ($\nu < 1.5$, say), these localized states grow in azimuthal extent in the same manner as localized states in the 1D cubic-quintic SH equation, but for larger subcriticality we found that they instead expand into the interior, forming wall-attached worm-like states similar to those present in the plane [37, 42].

It is significant, though not altogether surprising, that the structures we identified in this simple model problem resemble similar structures observed in fluid flows, combustion, laser physics, and indeed other spatially confined systems. Convection in a vertical cylinder provides the closest realization of these states despite the absence of subcriticality. Numerical continuation studies of this system [6, 7] in cylinders with moderately small aspect ratio identified not only target states but also nonaxisymmetric states with the symmetry D_2 , D_2^- , D_3 , D_4 , D_4^- and D_6^- . As in our case, some of these appear through a primary instability of the conduction state, while others appear through secondary bifurcations of axisymmetric states. In a similar vein, existing studies of porous medium binary fluid convection on a periodic domain with a square cross-section identified four-armed states with both D_4 and D_4^- symmetry [38, 39] and studied their snaking behavior as the arms grew in extent, ultimately interacting with their images.

Despite the wealth of new phenomena described here, a number of critical questions remain. Even in our stripped down problem it proved impossible to follow many of the solution branches all the way, and in larger domains it remains unclear whether the localized structures ever connect to a domain-filling state. The domain-filling transition of the wall state likewise remains to be fully characterized. Much of the interesting behavior of this system can be traced to the competition between stripes parallel to the wall or perpendicular to it. This competition is sensitive to both the domain radius R and the subcriticality parameter ν , and appears responsible for absence of a direct connection between the D_m -symmetric m -arm

states and axisymmetric target states. Nevertheless, this study should serve as a useful guide to subcritical pattern formation in a bounded 2D domain beyond the standard case of squares and rectangles with Neumann or periodic boundary conditions.

Appendix: The `pde2path` implementation

In its standard setting, the MATLAB package `pde2path` [25–27] uses the finite element method (FEM) to spatially discretize systems of second order PDEs, and combines this with a variety of numerical continuation and bifurcation algorithms, including some simple DNS. We therefore rewrite the 4th order SH equation (1) as a parabolic-elliptic system (for simplicity setting $q = 1$),

$$M_d \partial_t \begin{pmatrix} u_1 \\ u_2 \end{pmatrix} = \begin{pmatrix} -\Delta u_2 - 2u_2 - (1-\varepsilon)u_1 + f(u_1) \\ -\Delta u_1 + u_2 \end{pmatrix}, \quad (\text{A.1})$$

with a singular dynamical mass matrix $M_d = \begin{pmatrix} 1 & 0 \\ 0 & 0 \end{pmatrix}$, $f(u_1) = \nu u_1^3 - u_1^5$, and Neumann BCs for u_1 and u_2 . See, e.g., [26, Remark 8.1] for the equivalence of (1) and (A.1) over convex Lipschitz domains, or general domains with a smooth boundary. For the patterns studied here, it turns out that careful meshing [26, §4.1.1] is crucial to maintain symmetry of the solution branches, i.e., to mitigate branch jumping, and throughout this work we used axisymmetric meshes. Additionally, instead of the standard piecewise linear FEM we chose 6-node triangles [44, §5.1], i.e., piecewise quadratic elements. With these, a typical discretization of the $R = 14$ disk uses about 17 000 nodes, yielding a total of 34 000 degrees of freedom for (A.1).

The basic `pde2path` implementation can be found in [45], where the main script produces the radial, daisy and localized daisy branches. Additionally, movies illustrating the solutions along the branches explored in this paper are included in the SI.

ACKNOWLEDGMENTS

The work of NV and EK was supported in part by the National Science Foundation under grant DMS-1908891. NV was also funded by the National Agency for Research and Development (ANID) through the Scholarship Program: Becas de Postdoctorado en el extranjero, becas Chile 2018 No. 74190030.

-
- [1] R. Hoyle, *Pattern Formation: An Introduction to Methods* (Cambridge University Press, 2006).
 - [2] M. Cross and H. Greenside, *Pattern Formation and Dynamics in Nonequilibrium Systems* (Cambridge University Press, 2009).
 - [3] Y.-P. Ma and E. A. Spiegel, *Physica D* **240**, 150 (2011).

- [4] M. C. Cross and P. C. Hohenberg, *Rev. Mod. Phys.* **65**, 851 (1993).
- [5] B. Hof, P. G. J. Lucas, and T. Mullin, *Phys. Fluids* **11**, 2815 (1999).
- [6] K. Borońska and L. S. Tuckerman, *Phys. Rev. E* **81**, 036320 (2010).

- [7] K. Borońska and L. S. Tuckerman, Phys. Rev. E **81**, 036321 (2010).
- [8] F. Hébert, R. Hufschmid, J. Scheel, and G. Ahlers, Phys. Rev. E **81**, 046318 (2010).
- [9] D.-J. Ma, D.-J. Sun, and X.-Y. Yin, Phys. Rev. E **74**, 037302 (2006).
- [10] A. Palacios, G. H. Gunaratne, M. Gorman, and K. A. Robbins, Chaos **7**, 463 (1997).
- [11] D. Lo Jacono, A. Bergeon, and E. Knobloch, Combustion and Flame **176**, 117 (2017).
- [12] M. Sheintuch and O. Nekhamkina, J. Chem. Phys. **107**, 8165 (1997).
- [13] C. Degen, B. Krauskopf, G. Jennemann, I. Fischer, and W. Elsässer, J. Opt. B: Quantum Semiclass. Opt. **2**, 517 (2000).
- [14] H. F. Goldstein, E. Knobloch, I. Mercader, and M. Net, J. Fluid Mech. **248**, 583 (1993).
- [15] F. Zhong, R. E. Ecke, and V. Steinberg, J. Fluid Mech. **249**, 135 (1993).
- [16] B. Favier and E. Knobloch, J. Fluid Mech. **895**, R1 (2020).
- [17] K. Borońska and L. S. Tuckerman, J. Fluid Mech. **559**, 279 (2006).
- [18] M. Golubitsky, E. Knobloch, and I. Stewart, J. Nonlinear Sci. **10**, 333 (2000).
- [19] M. Dellnitz, M. Golubitsky, A. Hohmann, and I. N. Stewart, Int. J. Bif. Chaos **5**, 1487 (1995).
- [20] D. Lloyd and B. Sandstede, Nonlinearity **22**, 485 (2009).
- [21] S. McCalla and B. Sandstede, Physica D **239**, 1581 (2010).
- [22] J. J. Bramburger, D. Altschuler, C. I. Avery, T. Sangsawang, M. Beck, P. Carter, and B. Sandstede, SIAM J. Appl. Dyn. Syst. **18**, 1420 (2019).
- [23] J. Burke and E. Knobloch, Phys. Lett. A **360**, 681 (2007).
- [24] E. J. Doedel, A. R. Champneys, T. F. Fairgrieve, Y. Kuznetsov, B. Sandstede, and X. Wang, Auto 97: Continuation and bifurcation software for ordinary differential equations (with homcont), <https://github.com/auto-07p> (2002), technical report, Concordia University.
- [25] H. Uecker, D. Wetzel, and J. D. M. Rademacher, Numerical Mathematics: Theory, Methods and Applications **7**, 58 (2014).
- [26] H. Uecker, Numerical Continuation and Bifurcation in Nonlinear PDEs (SIAM, 2021).
- [27] H. Uecker, www.staff.uni-oldenburg.de/hannes.uecker/pde2path (2020).
- [28] J. D. Crawford, M. Golubitsky, M. G. M. Gomes, E. Knobloch, and I. N. Stewart, Boundary conditions as symmetry constraints, in *Singularity Theory and its Applications, Warwick 1989, Part II* (Springer, 1991) pp. 63–79.
- [29] U. Thiele, A. J. Archer, M. J. Robbins, H. Gomez, and E. Knobloch, Phys. Rev. E **87**, 042915 (2013).
- [30] J. D. M. Rademacher and A. Scheel, Int. J. Bif. Chaos **17**, 2679 (2007).
- [31] J. D. M. Rademacher, B. Sandstede, and A. Scheel, Physica D **229**, 166 (2007).
- [32] U. Thiele, LINDROP: Linear stability of steady solutions of a thin film equation for a horizontal homogeneous substrate, <https://www.uni-muenster.de/CeNoS/Lehre/Tutorials/continuation.html> (2014), online tutorial.
- [33] I. Mercader, O. Batiste, A. Alonso, and E. Knobloch, Phys. Rev. E **80**, 025201R (2009).
- [34] S. M. Houghton and E. Knobloch, Phys. Rev. E **80**, 026210 (2009).
- [35] H.-C. Kao and E. Knobloch, Dynamical Systems **28**, 263 (2013).
- [36] A. Bergeon, J. Burke, E. Knobloch, and I. Mercader, Phys. Rev. E **78**, 046201 (2008).
- [37] D. Avitabile, D. J. B. Lloyd, J. Burke, E. Knobloch, and B. Sandstede, SIAM J. Appl. Dyn. Syst. **9**, 704 (2010).
- [38] D. Lo Jacono, A. Bergeon, and E. Knobloch, J. Fluid Mech. **730**, R2 (2013).
- [39] D. Lo Jacono, A. Bergeon, and E. Knobloch, Fluid Dyn. Res. **49**, 061402 (2017).
- [40] M. Le Berre, A. S. Petrescu, E. Ressayre, and A. Tallet, Opt. Comm. **123**, 810 (1996).
- [41] J. Burke and E. Knobloch, Discrete and Continuous Dyn. Syst. Suppl. , 109 (2009).
- [42] D. J. B. Lloyd, SIAM J. Appl. Dyn. Syst. **18**, 1892 (2019).
- [43] B. B. Plapp and E. Bodenschatz, Physica Scripta **T67**, 111 (1996).
- [44] C. Pozrikidis, *Introduction to finite and spectral element methods using MATLAB®*, 2nd ed. (CRC Press, Boca Raton, FL, 2014).
- [45] N. Verschuere, Pattern formation on a finite disk using the SH35 equation, <https://nverschuere.bitbucket.io/sh35p2p.html> (2021), online tutorial.